

A beehive-shaped Pd and Ni Nanoparticle Composite Showing Significant Electrocatalytic Activity Towards Ethanol Oxidation Reaction (EOR)

Keqiang Ding^{1,2,*}, Fujuan Shi¹, Dongyue Zhang¹, Boxia Li¹, Jiasheng Chen¹, Mengyao Di¹, Mengying Yan¹, Hui Wang²

¹ Hebei Key Laboratory of Inorganic Nano-materials, Hebei Key Laboratory of Organic Functional Molecules, College of Chemistry and Materials Science, Hebei Normal University, Shijiazhuang, 050024, China

² Hebei LingDian New Energy Technology Co., Ltd, Tangshan, 064200, China

*E-mail: dkeqiang@263.net

Received: 10 December 2021 / Accepted: 26 January 2022 / Published: 4 March 2022

For the first time, a beehive-shaped palladium and nickel (Pd_xNi_y) nanoparticle composite electrocatalyst for ethanol oxidation reaction (EOR) was prepared via a pyrolysis method using palladium oxide and the calcined product of a nickel acetylacetonate (NAA) as the starting materials. Firstly, a proper amount of NAA was respectively calcined at 300 °C, 500 °C and 700 °C for 2 h in an air atmosphere producing three nickel-containing precursors, successively being employed to prepare the final sample of catalyst c_1 , c_2 and c_3 . As displayed by the SEM images, c_1 , c_2 and c_3 , respectively, delivered a rock-shaped, beehive-shaped and scorched earth-shaped morphology. As revealed by the TEM images, all resultant catalysts were accumulated by a large number of nanoparticles. XRD and XPS results strongly indicated that metallic Pd, PdO, NiO, metallic Ni and carbon materials were the main components of all as-prepared catalysts. More than that, as verified by the CV test, compared to other two catalysts, c_2 exhibited a significant electrocatalytic activity towards EOR, that is, the EOR current density of the forward peak (25 mA cm^{-2}) measured on c_2 at 50 mV s^{-1} , was almost 28 times higher than that of EOR on c_3 (0.9 mA cm^{-2}). Especially, the Faraday current density of EOR on c_2 at 600 s, as demonstrated by the CA measurement, was as large as 16.5 mA cm^{-2} , remarkably higher than that of EOR recorded on c_1 (4.2 mA cm^{-2}) and c_3 (0.15 mA cm^{-2}). Developing a novel kind of nickel-containing precursor and preparing a beehive-shaped high performance Pd_xNi_y electrocatalyst for EOR were the main dedications of this preliminary work, which was very beneficial to the further exploration of Pd-based electrocatalysts.

Keywords: calcined products; Pd_xNi_y composite nanoparticles; beehive-shaped morphology; pyrolysis method; ethanol oxidation reaction

1. INTRODUCTION

Nowadays, with the tendency of global warming, how to greatly reduce carbon dioxide emissions has become one of the key challenges in the process of sustainable human development [1]. Generally, the wide utilization of fuel vehicles is thought as one main reason of producing carbon dioxide [2, 3]. Therefore, replacing fuel vehicles with electric vehicles (EV), especially in recent years, is announced as a national strategy by many countries so as to greatly lower the emissions of carbon dioxide achieving the goal of peak carbon dioxide emissions as well as carbon neutrality as soon as possible [4]. Consequently, battery, because of its irreplaceable role in an EV, has been paid unprecedented research attention recently. Among all existing batteries, ethanol-fed battery, namely direct ethanol fuel cells (DEFCs), mostly owing to its higher safety and environment benign as well as higher theoretical energy density of 8 kWh kg^{-1} , is reckoned as one of the most suitable batteries to power an EV[5,6]. Therefore, ethanol oxidation reaction (EOR), an electrochemical reaction that can release electrons at the anode part of a DEFC, has aroused widespread researching concern in the last several years [7, 8]. Correspondingly, developing new EOR catalysts with high efficiency and low cost has become a hot topic in the EOR related catalysis field. Of late, besides the platinum (Pt)-based catalysts, palladium (Pd)-based catalysts were also, especially in alkaline medium, indicated to have an evident electrocatalytic activity towards EOR. Therefore, Pd-based catalysts, mainly thanks to the abundant Pd reserves relative to that of Pt, have received ever increasing attention particularly in the field of DEFCs-related catalysts.

Lately, to further reduce the catalyst cost, numerous novel kinds of Pd-based catalysts, such as Pd-based binary catalyst like Pd-Ag[9], Pd-Zn[10] as well as Pd-based ternary catalysts like Au-Ag-Pd[11] and PdAuCu [12], have been successfully prepared with an intention to substitute for the pure Pd catalyst. Among all existing Pd-based catalysts, Pd and Ni (Pd-Ni) composite catalyst, mainly due to its higher electrocatalytic performance towards EOR and its relatively lower preparation cost, has attracted much researching attention in recent years [13]. To our knowledge, many Ni-containing substances have been successfully employed as the Ni sources to prepare Pd-Ni composite catalysts. For example, Yi's group [14] chemically prepared a Pd-Ni binary nanocatalyst where $\text{Ni}(\text{NO}_3)_2 \cdot 6\text{H}_2\text{O}$ and $\text{N}_2\text{H}_4 \cdot \text{H}_2\text{O}$ were used as the nickel precursor and reducing agent, respectively. And in Yi's work [14], a large number of huge aggregations rather than the regular particles were seen clearly in the resultant SEM images. The research team led by Gojković [15] skillfully prepared a Pd-Ni/C catalyst via a two-step procedure, namely, a non-noble metal was firstly chemically deposited on a carbon support and then the as-prepared sample was covered by a noble metal. And in their works, in order to prepare the metallic Ni, $\text{Ni}(\text{HCOO})_2$ as the nickel-containing substance was deliberately reduced by a conventional reducing agent of NaBH_4 . Zhang's group [16] successfully prepared a Pd-Ni-P composite catalyst where $\text{NiCl}_2 \cdot 6\text{H}_2\text{O}$ was utilized as the nickel precursor. Very recently, Wang's team [17] fabricated mesoporous nanoparticles assembled PdNi/Ni nanotubes through using nickel nano-wires as the sacrificial template. And in Wang's work [17], nickel nano-wires were cleverly prepared employing NiCl_2 , $\text{C}_2\text{H}_6\text{O}_2$ and $\text{N}_2\text{H}_4 \cdot \text{H}_2\text{O}$ as the starting materials. Although many kinds of nickel-containing substances are selected as the nickel sources to prepare Pd-Ni composite particles, to the best of our knowledge, the calcined products of Ni-containing organic compounds are rarely used as the starting

materials of Ni-containing precursor for producing Pd-Ni particle composites.

In addition, besides the chemical compositions, the surface morphology and the internal structure of an electrocatalyst are also important factors which can remarkably influence the electrocatalytic performance of an electrocatalyst prepared. To our knowledge, in recent years, several novel configurations of the Pd-Ni composite particles have been successfully developed with an intention to further promote their electrocatalytic activities. For instance, Lu's group [18] skillfully immobilized spherical palladium nanoparticles, reduced graphene oxide and polydopamine together onto the surface of a nickel foam substrate creating a special three-dimensional frame structure. Nguyen's group [19] deposited Pd layers on Ni nanowires in a polyol medium through employing a novel galvanic replacement reaction method generating a Pd-coated Ni nanowire electrocatalyst. Yavari's group [20] firstly synthesized spongy nickel oxides (SNO) using a solution combustion method, and then nanoraspberry-like palladium nanoparticles were prepared onto the as-prepared SNO via a chemical reaction, producing a novel SNO-supported Pd nanoparticle catalyst for EOR. In Yavari's work, PdCl₂ and NaBH₄ were employed as the reactants in the preparation of anoraspberry-like palladium nanoparticles. Except for above newly prepared Pd-Ni composite particles, the synthesis of flower-like Pd electrocatalysts supported on Ni nanowire arrays [21] as well as the fabrication of spherical-like shape PdNi catalysts [22] has also been well described in the previously published works. However, as far as we know, the preparation of Pd-Ni composite nanoparticle catalysts with a well-defined beehive-shaped morphology was scarcely reported so far.

In this work, firstly, a proper amount of NAA was sintered at an elevated temperature in an air atmosphere for 2 h to harvest the final calcined products. The calcined products of NAA calcined at 300 °C, 500 °C and 700 °C were, respectively, nominated as precursor NAA-300, NAA-500 and NAA-700. And then, 20 mg of NAA-300 and 20 mg of PdO·H₂O were added together in 10 mL of double distilled water under vigorous stirring to form a suspension solution, soon afterwards, the resultant suspension solution was transferred in a well-sealed autoclave to accomplish the pyrolysis process. The pyrolysis temperature and the pyrolysis time were 200 °C and 3h, respectively. The catalysts prepared in the presence of NAA-300, NAA-500 and NAA-700 were, respectively, denoted as catalyst c₁, c₂ and c₃. As exhibited by the SEM images, a beehive-shaped surface morphology was delivered by c₂. More importantly, c₂ exhibited the best electrocatalytic activity for EOR among all prepared catalysts. To one's surprise, the diffraction peak assigned to metallic Ni rather than metallic Pd was displayed in the XRD pattern of c₂, which was a novel finding for the Pd-based binary nanoparticle composites based on our literature survey. Meanwhile, in this work, no carriers of catalyst were deliberately introduced in the catalyst preparation process since the calcined product acted as the nickel source and the catalyst support as well.

2. EXPERIMENTAL DETAILS

2.1 Reagents and materials

Nickel acetylacetonate (NAA) and other chemical reagents were used as purchased, and all

electrodes were bought from Tianjin Aida Co., Ltd (China). The solution consisting of 1 M KOH and 1 M C₂H₅OH was the electrolyte solution used for measuring the electrocatalytic performances of all as-synthesized catalysts towards EOR. It was worth emphasizing that, to eliminate the influence of chloride ion dissolved in water, all aqueous solutions were carefully prepared by using double distilled water.

2.2 Preparation of palladium and nickel composite nanoparticles

Firstly, three novel Ni-containing precursors were prepared via an air atmosphere calcination method. That is, a proper amount of NAA (light green solid powder) was directly calcined at 300 °C for 2 h in a muffle furnace under the air atmosphere to produce a nickel-containing precursor. To study the influence of the calcination temperature on the physicochemical properties of the prepared precursors, three different calcination temperatures were employed in preparing the Ni-containing precursors. And, the precursors calcined at 300 °C, 500 °C and 700 °C were identified as NAA-300, NAA-500 and NAA-700, respectively. Next, 0.02 g of NAA-300 and 0.02 g of PdO·H₂O were added together in 10 mL double distilled water generating a suspension solution, and then the resulting suspension solution was placed in a well-sealed autoclave which was heated in a blast drying oven at 200 °C for 3 h to end the pyrolysis process. After being cooled down to the room temperature, the as-obtained solid substances were carefully washed with double distilled water and dried in air for 5 h to acquire the final samples. The preparation conditions of other two samples were identical to that of above sample except for using various precursors. The samples synthesized with NAA-300, NAA-500 and NAA-700 were, respectively, labeled as catalyst c₁, c₂ and c₃.

2.3 Preparation of Pd_xNi_y catalysts modified glassy carbon (GC) electrodes

Firstly, a suspension solution containing 2 mg of c₁ and 0.5 mL of Nafion ethanol solution was carefully prepared in which the Nafion mass content of the Nafion ethanol solution was about 0.1 wt.%. And then, the resultant suspension solution was treated by ultrasonic vibration for 1 h so as to produce a well-dispersed catalyst ink. After that, 12 μL of the as-formed catalyst ink was dropped on the cross-section of a well-treated GC electrode (The diameter of the cross-section was 3 mm). And then, after being well dried in air, a catalyst modified GC electrode was successfully prepared. The GC electrodes modified with c₁, c₂ and c₃ were called as electrode c₁, c₂ and c₃, respectively.

2.4 Characterization

The crystal phase as well as the chemical composition of all as-prepared samples was carefully examined by XRD (X-ray diffraction) measurement using a X-ray diffractometer (Bruker D8 ADVANCE X-ray diffractometer (Cu K α source, $\lambda = 0.154$ nm)). Scanning electron microscopy (SEM, HITACHI, S-570) and transmission electron microscopy (TEM, HITACHI, H-7650) were employed, respectively, to observe the surface morphology of the prepared samples and to estimate the particle

size of the as-prepared nanoparticles. Energy dispersive X-ray spectroscopy (EDS, PV-9900, USA) was used to ascertain both the element kinds and the approximate element contents of all resultant catalysts. The functional groups of all studied samples were further investigated by using Fourier transform infrared spectrometry (FTIR) (Hitachi FTIR-8900 spectrometer, Japan). To exactly confirm the kinds of chemical substances, the element chemical valences of the as-synthesized samples were also examined by using X-ray photoelectron spectroscopy (XPS, Kratos Analytical spectrometer, Al K_{α} radiation).

All the electrochemical measurements were conducted by using a conventional three-electrode cell on an electrochemical workstation (CHI 660E, Shanghai Chenhua Apparatus, China) in which the main electrochemical techniques were cyclic voltammetry (CV), chronoamperometry (CA) and EIS (electrochemical impedance spectroscopy). In the conventional three-electrode cell, the catalyst modified GC electrode, a platinum (Pt) wire and a saturated calomel electrode (denoted as SCE) were, respectively, utilized as the working electrode, the counter electrode and the reference electrode. All potential values reported in this work were the potential separation between the electrode potential of the working electrode and the electrode potential of the SCE. The electrolyte solution used for evaluating the electrocatalytic activities of all as-prepared catalysts towards EOR was a solution containing 1M ethanol and 1M KOH. No special protections were employed while operating above electrochemical measurements, and all the experiments were carried out at room temperature.

3. RESULTS AND DISCUSSION

3.1 Characterizations of all as-prepared samples

The XRD patterns for all calcined products as well as the standard XRD pattern for both metallic Ni and NiO are illustrated in figure a of Fig.1a. Evidently, No diffraction peaks were exhibited in the XRD pattern of NAA-300 which strongly indicated that no substances with higher crystallinity were prepared in the calcined product of NAA-300, which should be mainly attributed to the lower calcination temperature at which no crystal materials were produced.

For NAA-500, the diffraction peaks positioned at 44.6° , 51.9° and 76.6° were, respectively, assigned to the (111), (200) and (220) crystal face of metallic Ni (JCPDS, No.04-0850) [23] which substantially demonstrated that metallic Ni as the main crystal substance existed in NAA-500 after the air calcination process. In the case of NAA-700, besides the diffraction peaks indexed as the metallic Ni, the diffraction peaks assigned to NiO were also clearly displayed, namely, the diffraction peaks located at 37.3° , 43.4° , 62.9° , 75.6° and 79.4° , respectively, corresponded well to the (111), (200), (220), (311) and (222) crystallographic plane of NiO (JCPDS, No.47-1049) [23]. Also, the positions of the diffraction peaks for NiO of NAA-700 were shifted slightly towards higher 2θ value relative to that of the diffraction peaks in the standard NiO XRD patterns.

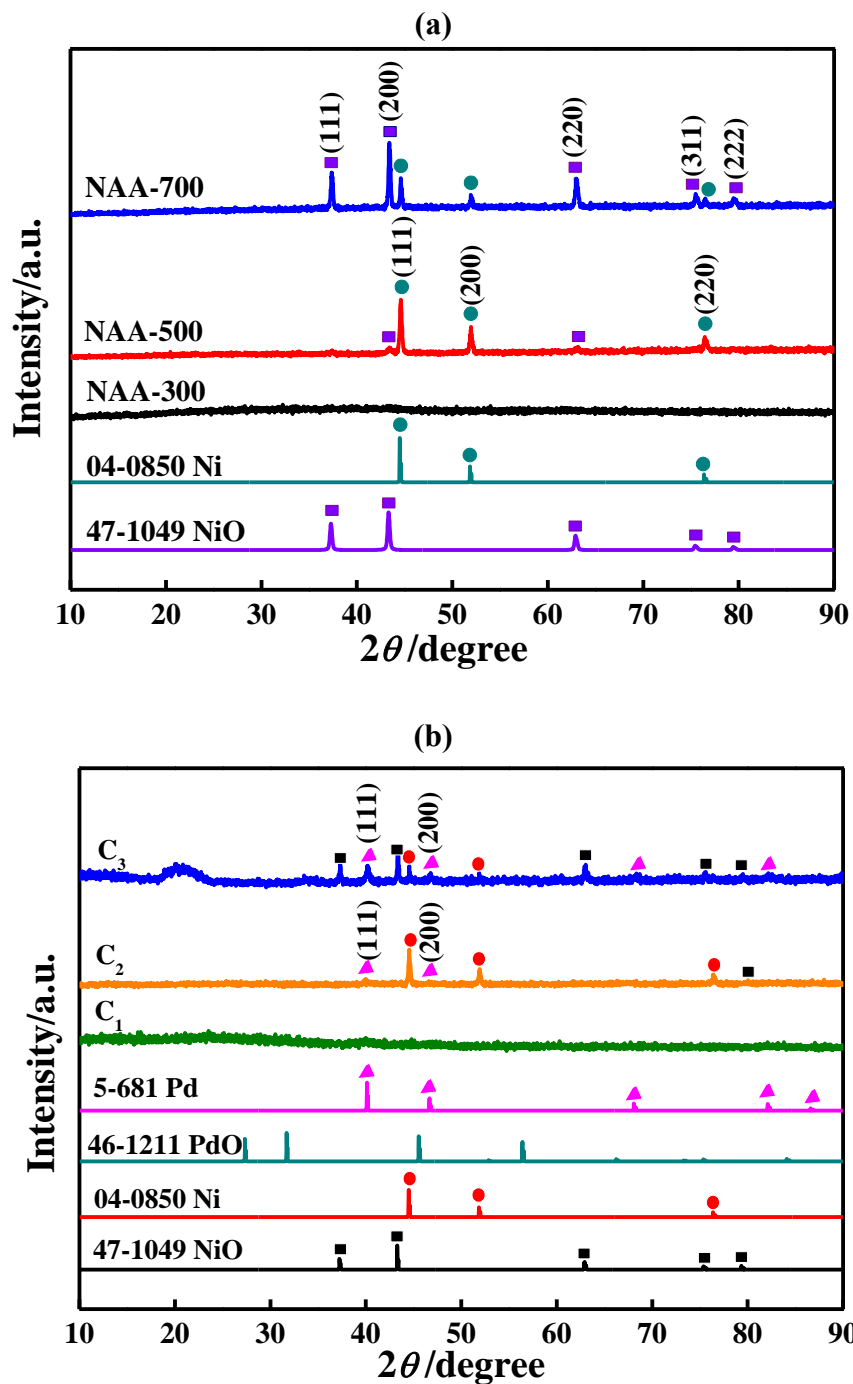


Figure 1a. (a) XRD patterns of NAA-300, NAA-500 and NAA-700 as well as the standard XRD patterns for both metallic Ni and NiO. (b) XRD patterns for catalyst c₁, c₂ and c₃ as well as the standard XRD patterns of Pd, PdO, Ni and NiO.

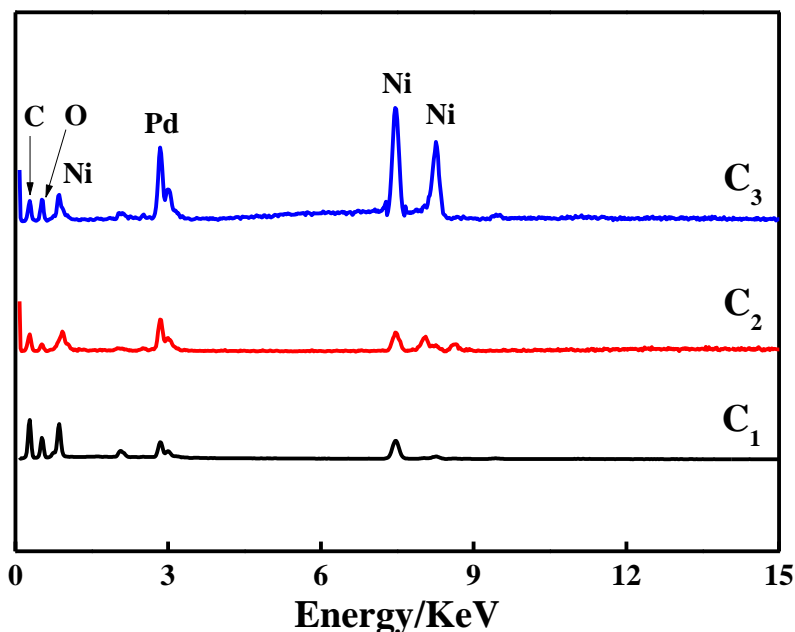
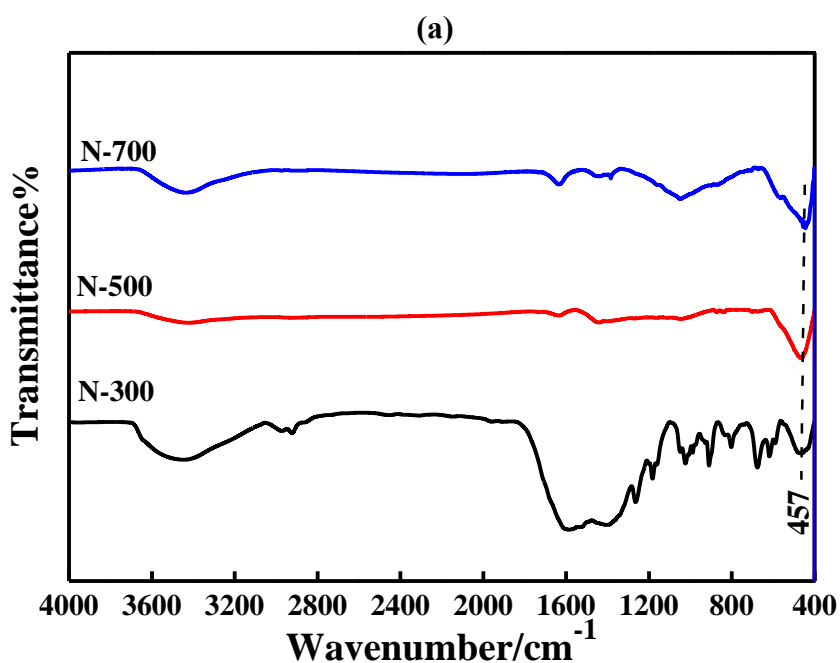


Figure 1b. EDS patterns for catalyst c_1 , c_2 and c_3 .

For instance, the 2θ value (37.3°) of the diffraction peak assigned to the (111) lattice plane for NiO of NAA-700 was somewhat larger than that (37.2°) of the (111) lattice plane of the standard NiO XRD patterns. The shifting of the 2θ value of the diffraction peak towards higher 2θ values was generally originated from the crystal lattice contraction [24], that is, compared to the case of pure NiO, the unit cell of NiO was partially replaced by Ni producing a reduced unit cell volume [24].



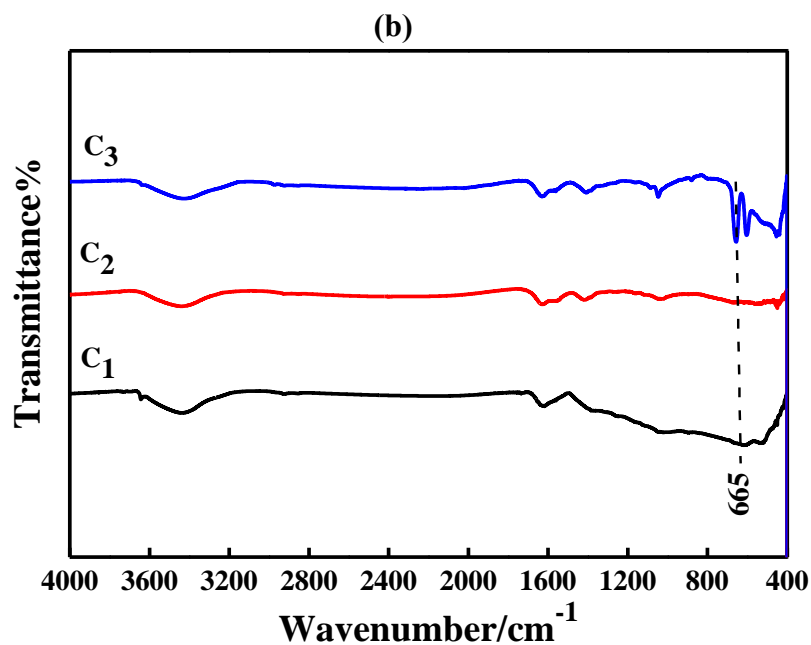


Figure 1c. (a) FTIR spectra for the calcined products of NAA-300, NAA-500 and NAA-700. (b) FTIR spectra for catalyst c_1 , c_2 and c_3 .

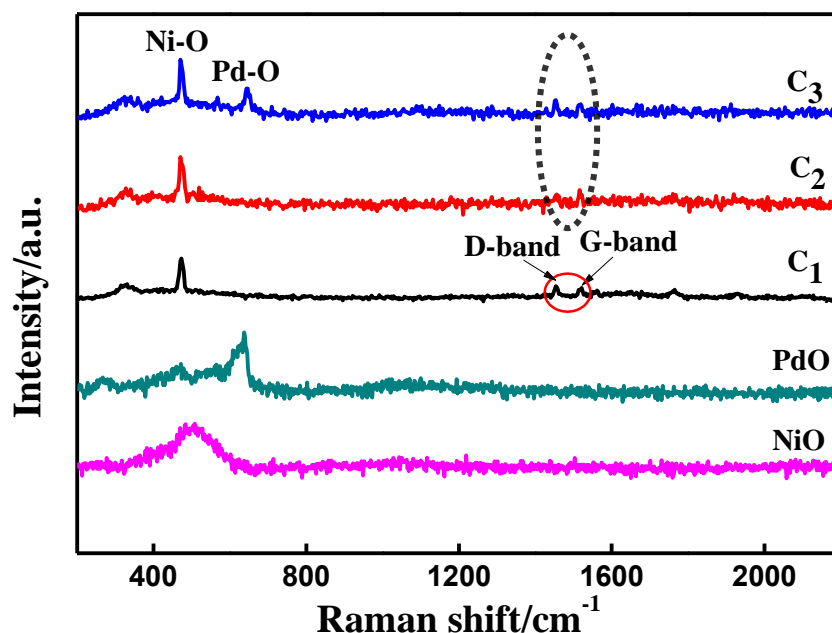


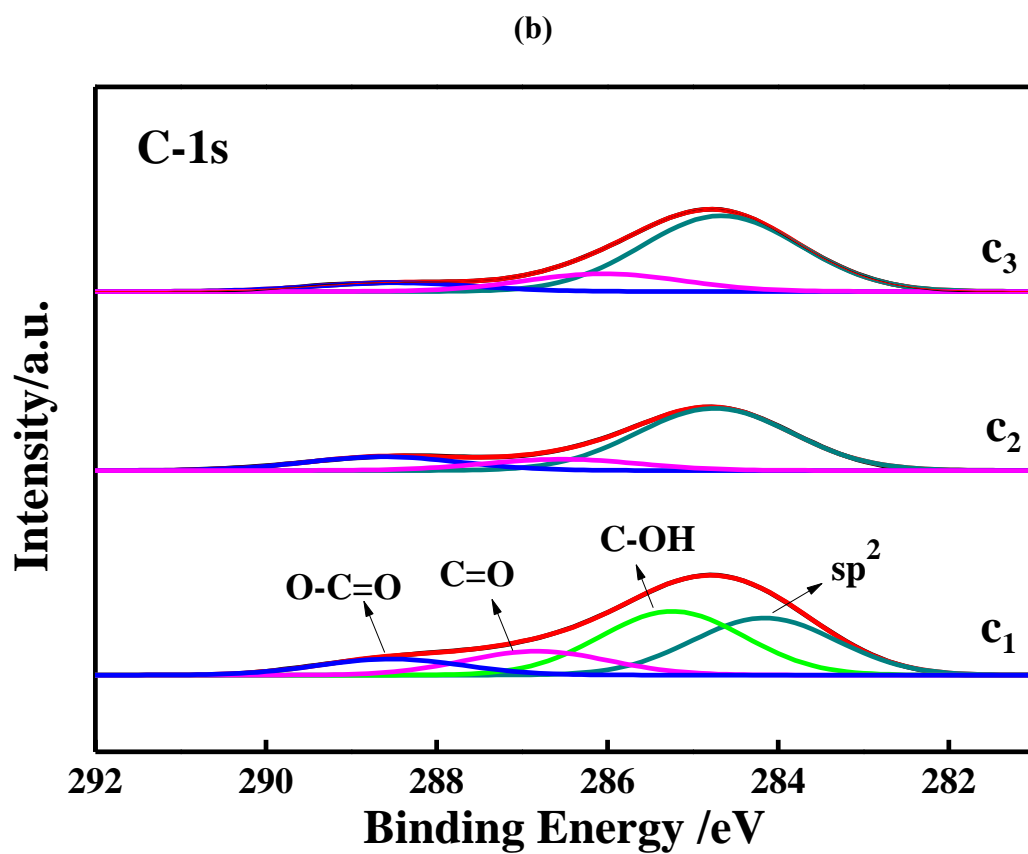
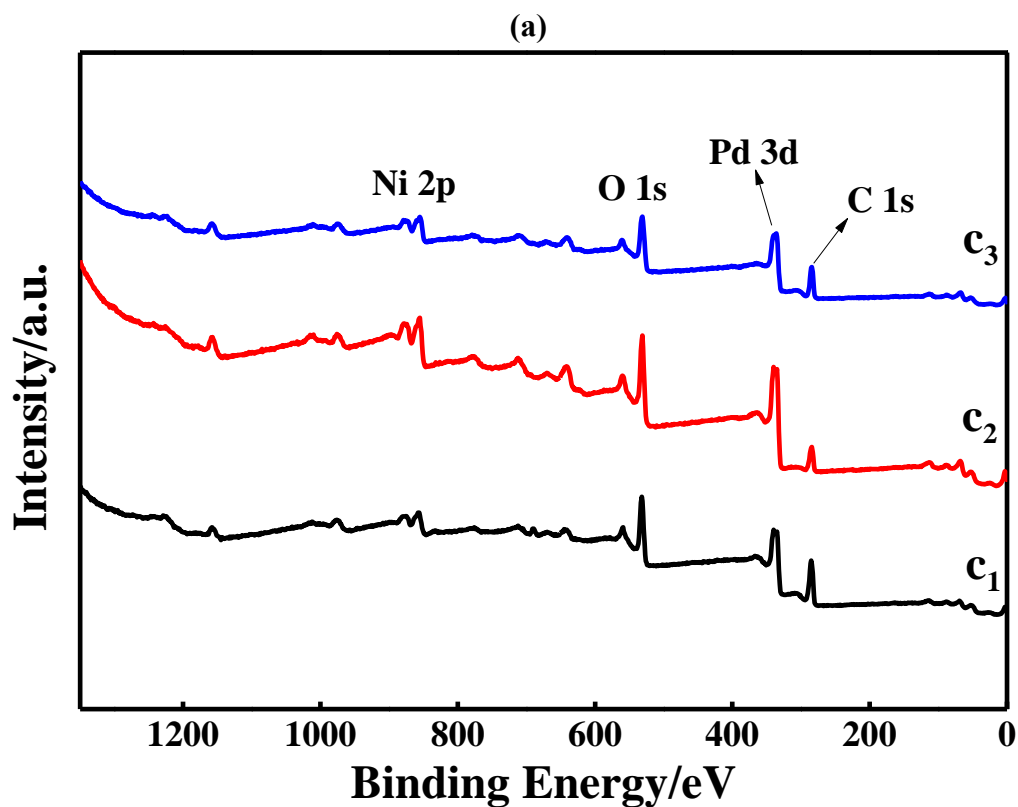
Figure 1d. Raman spectra for catalyst c_1 , c_2 and c_3 .

The XRD patterns, including the standard XRD patterns for metallic Pd, PdO, metallic Ni and NiO, of all as-prepared catalysts are given in figure b of Fig.1a. Similar to the case of NAA-300, no evident diffraction peaks were displayed in the whole 2θ angle region of the XRD patterns for c_1 suggesting that no crystal materials were formed in c_1 . Interestingly, for c_2 , only three diffraction peaks belonging to the metallic Ni rather than the metallic Pd were distinctly exhibited which effectively indicated that metallic Ni was still the main crystal material of c_2 . While, for c_3 , except for the

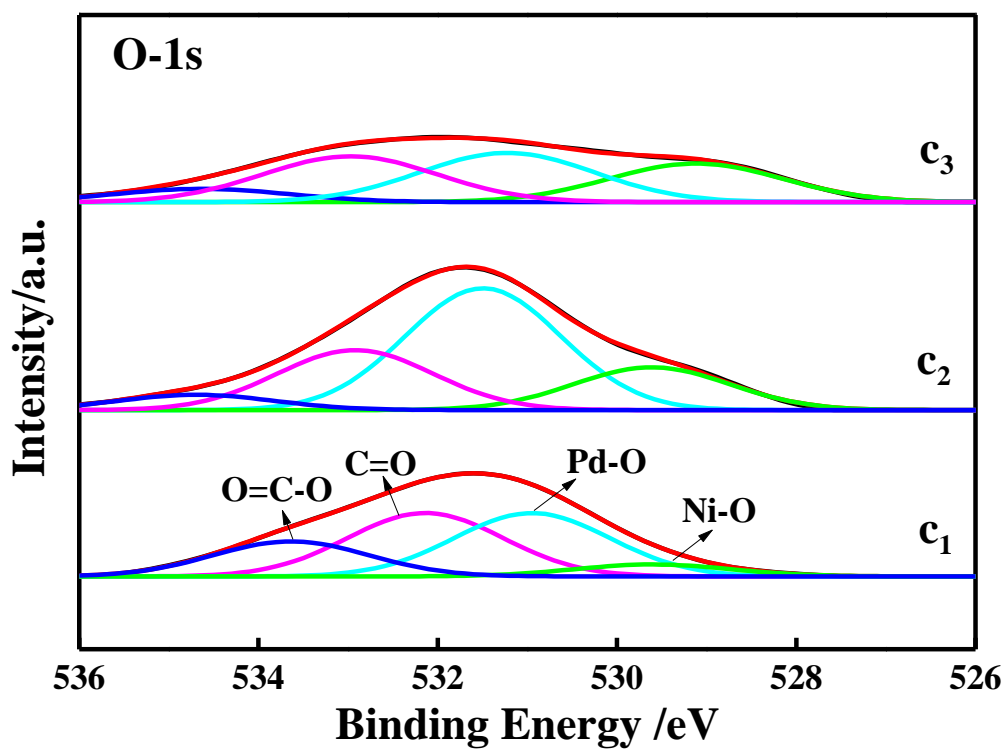
diffraction peaks assigned to both NiO and metallic Ni, the diffraction peaks attributable to the metallic Pd were also visible, namely, the diffraction peaks centered at 40.0° and 46.6° were respectively indexed as the (111) and (200) facet of metallic Pd [25], which at least indicated that NiO, Ni and Pd were prepared in c_3 after the very simple pyrolysis process. Unfortunately, the diffraction peaks attributed to PdO were not displayed in the XRD patterns of c_3 which was probably due to its very limited amount in c_3 . Also, a broad and weak diffraction peak was exhibited at about 20.6° in the XRD pattern of c_3 which was mostly attributed to the existence of amorphous carbon in c_3 [26]. As far as we know, the diffraction peaks indexed as metallic Pd were always exhibited as the main diffraction peaks in the XRD patterns of Pd-based catalysts in the previously published works [27, 28]. That is, in this work, no evident diffraction peaks assigned to the metallic Pd were observed in the XRD patterns of the resultant Pd-based catalysts, a novel finding to our knowledge.

EDS spectra for all synthesized catalysts are illustrated in Fig.1b. In each EDS pattern, the peaks assigned to C, O, Ni and Pd elements were all exhibited distinctly suggesting that all prepared catalysts were a composite material rather than a pure substance. The atomic percentages of Ni and Pd in c_1 , c_2 and c_3 were approximately detected to be 20.7% and 5.6%, 25.1% and 13.4%, 79.5% and 4.6%, respectively. As expected, the atomic content of Ni in all prepared catalysts evidently increased with elevating the calcination temperature which implied that more amounts of carbon elements of NAA have been consumed in the calcination process under the higher calcination temperature. And the atomic ratios of Ni to Pd were, respectively, roughly estimated to be 4:1, 2:1 and 16:1 for c_1 , c_2 and c_3 . That is, the largest Pd atomic content was delivered by c_2 . Apparently, for all resultant catalysts, the content of Ni was greatly higher than that of Pd, which was very meaningful to the preparation cost reduction of the Pd-based catalysts. Also, the atomic contents of C and O were approximately measured to be 14.5% and 59.1%, 24.5% and 36.9%, 6.9% and 9.2% in c_1 , c_2 and c_3 , respectively. That is to say, some carbon materials as the calcined ashes of NAA were remained in all as-synthesized catalysts, which was advantageous to the electrical conductivity improvement of an electrocatalyst [29].

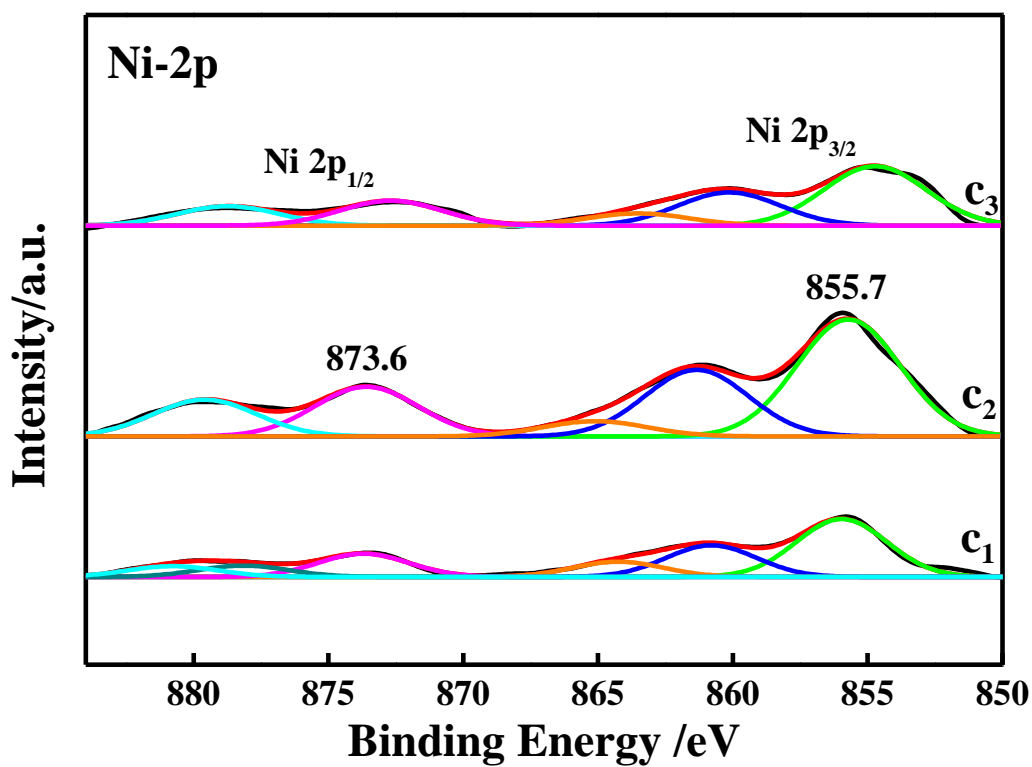
FTIR spectra for the calcined products as well as all synthesized catalysts are summarized in Fig.1c. For all calcined products (figure a of Fig.1c), a broad absorption peak centered at about 3445 cm^{-1} was observed exactly which strongly indicated the existence of hydroxyl (-OH) group in all produced precursors [30]. For NAA-300, several huge and broad absorption bands were explicitly displayed in the wavenumber region ranging from 1079 cm^{-1} to 1837 cm^{-1} which substantially indicated that carbon materials containing some organic functional groups were the main substances of NAA-300. For example, the absorption bands positioned at about 1601 cm^{-1} and 1393 cm^{-1} were assigned to the stretching vibrations of C=O [30, 31] and C-O[32], respectively. In contrast, no huge absorption bands assigned to organic functional groups were presented in the FTIR spectra for both NAA-500 and NAA-700, indicating that the amount of organic substances decreased remarkably with increasing the calcination temperature, being well in accordance with the EDS results (Fig.1b). Additionally, for all calcined products, an evident absorption peak at around 457 cm^{-1} was displayed clearly which was generally attributable to the presence of the stretching vibrations of Ni-O bonds [33].



(c)



(d)



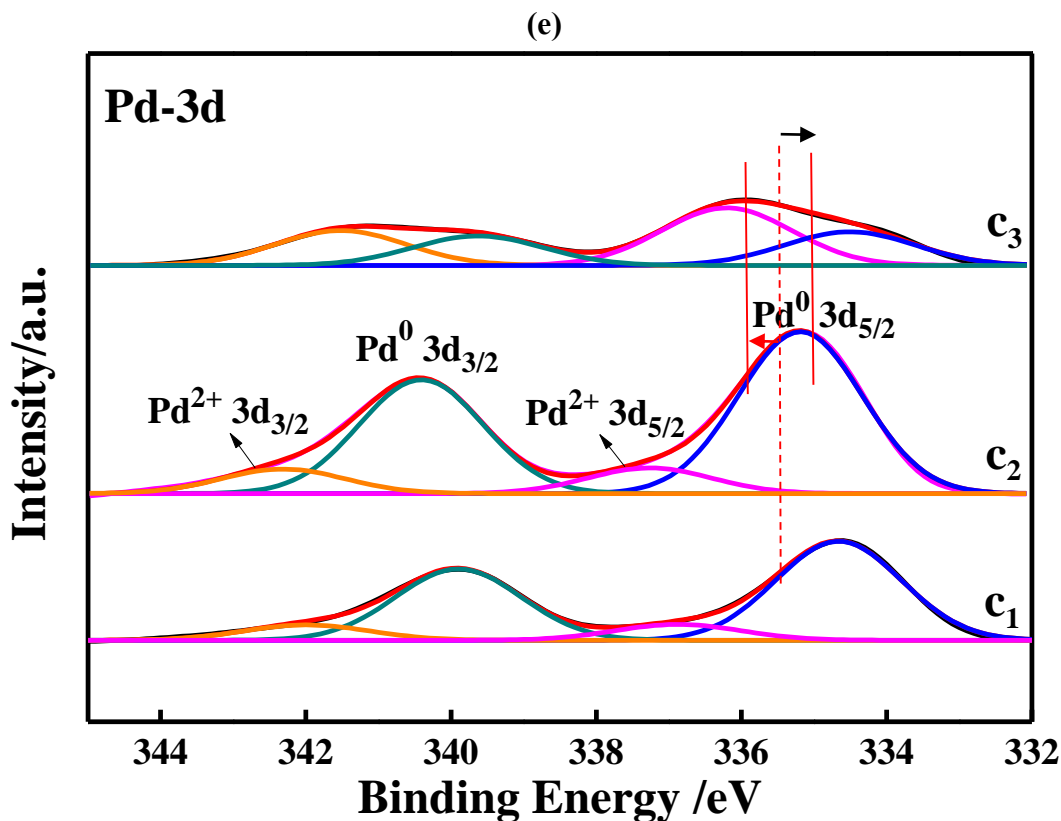


Figure 2. XPS survey spectra of c_1 , c_2 and c_3 . (a) Wide scan XPS survey spectra; (b) High resolution C1s spectra; (c) High resolution O1s spectra; (d) High resolution Ni 2p spectra; (e) High resolution Pd 3d spectra.

Thus, it was preliminarily concluded based on the FTIR spectra that nickel oxides were the main metal oxides of the calcined products of NAA. As shown by figure b of Fig.1c, for all prepared catalysts, the huge absorption band appearing in NAA-300 almost disappeared in the FTIR spectra. Similar to the case of figure a of Fig.1c, the absorption peak at about 3445 cm^{-1} was originated from the bending vibrations of -OH, and the absorption bands located at 1601 cm^{-1} and 1393 cm^{-1} were respectively ascribed to the presence of C=O [31] and C-O[32]. Interestingly, in this case, a novel absorption peak at 665 cm^{-1} assigned to Pd-O bond was observed in all prepared catalysts which effectively indicated that the starting material of PdO as one main component still existed in all as-synthesized catalysts.

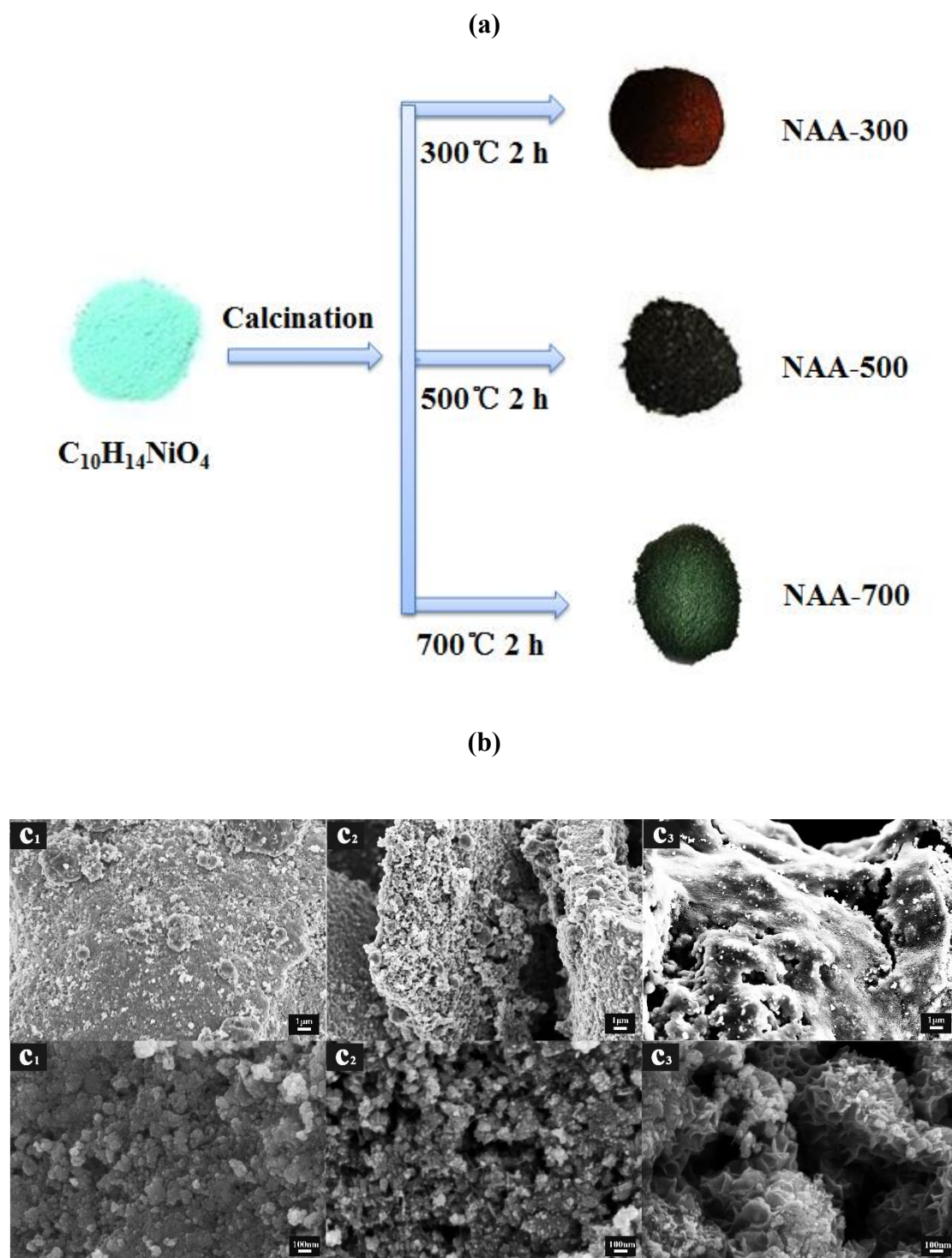
To further confirm the chemical components of all prepared catalysts, the Raman spectra results of all synthesized catalysts, including the Raman spectra for both the pure PdO and NiO, are given in Fig.1d. Evidently, the sharp peak appearing at 467 cm^{-1} should be assigned to the Ni-O bond, implying the presence of NiO in all synthesized catalysts. For c_3 , an evident peak appeared at 640 cm^{-1} strongly indicating the existence of PdO in c_3 , which accorded well with the FTIR result of c_3 (figure b of Fig.1c). However, no distinct peaks assigned to PdO were found in the Raman spectra for both catalyst c_1 and c_2 . Additionally, in the case of c_1 , two small obvious peaks were exhibited at 1453 cm^{-1} and 1520 cm^{-1} , respectively, corresponding to the D-band and G-band of carbon materials, further corroborating the existence of carbon materials in c_1 [30]. As shown by the black dotted circle, above

two small peaks were also evidently exhibited in the Raman spectra for c_2 and c_3 , effectively affirming the presence of carbon materials.

XPS measures were conducted with an intention to further ascertain the chemical components of all prepared catalysts (Fig.2). In the wide scan XPS spectra (figure a) of the three prepared catalysts, the characteristic peaks ascribed to Ni, O, Pd and C elements were all displayed being well consistent with the EDS results (Fig.1b). In the C1s XPS spectra (figure b), several peaks were exactly presented indicating that carbon material as one main substance existed in all prepared catalysts. For c_1 , four binding energy (BE) peaks were distinctly exhibited which strongly suggested that four kinds of C existed in c_1 . That is, BE peaks at 284.2, 285.3, 286.9 and 288.6 eV were, respectively, attributed to the carbon of sp^2 -C (C=C) [34], C-OH [35], C=O [35] and O-C=O [35]. While for c_2 and c_3 , the BE peak assigned to the carbon of C-OH totally disappeared which could only be attributed to the higher calcination temperature. In addition, the BE peak intensity as well as the BE peak area of C1s XPS spectra for c_1 was prominently larger than that of c_2 and c_3 , implying that the content of carbon material in c_1 was higher as compared to that of other catalysts. As shown by figure c of Fig.2, four BE peaks were clearly displayed in each O1s XPS pattern suggesting that four types of O atom existed in all prepared catalysts. Taking c_1 as an example, the BE peak centered at 529.4, 530.9, 532.1 and 533.6 eV were generally originated from the oxygen atom of Ni-O [36], Pd-O[37], C=O[26] and O=C-O[26], respectively. That is, oxygen-containing carbon materials and metal oxides were the main substances of all synthesized catalysts. The Ni 2p XPS spectra of all prepared catalysts are given in figure d of Fig.2. Apparently, for all catalysts, the high resolution Ni 2p XPS spectra were deconvoluted into five BE peaks, and the BE peaks at 855.7 eV and 873.6 eV were respectively assigned to $2p_{3/2}$ and $2p_{1/2}$ of Ni(II) in NiO[38]. Other BE peaks in Ni 2p XPS spectra were usually identified as multi-electron excitation satellite peaks derived from Ni(II) ions during XPS measurement[38]. As illustrated in figure e of Fig.2 (Pd 3d XPS spectra), the BE peak intensity of c_2 was rather higher than that of c_1 and c_3 , strongly implying that more amount of Pd-based substances were prepared in c_2 , being consistent well with the EDS results (Fig.1b). For c_2 , the BE peaks located at 335.2 eV and 340.4 eV were attributed to the orbit of Pd^0 ($3d_{5/2}$) and Pd^0 ($3d_{3/2}$) [14, 19, 39], respectively, corroborating the existence of metallic Pd in c_2 . And the small BE peaks appearing at 337.6 eV and 342.4 eV were, respectively, stemmed from the presence of Pd^{2+} ($3d_{5/2}$) and Pd^{2+} ($3d_{3/2}$) [14], being attributed to the existence of Pd^{2+} in PdO. Also, the shifting of the BE peak position was observed clearly. For instance, compared to the BE peak of Pd^0 ($3d_{5/2}$) at 334.6 eV for c_1 , the position of the same BE peak for c_2 was positively shifted for 0.6 eV (335.2 eV) which was beneficial to weaken the adsorption energy for intermediates [17]. While, the position of the same BE peak for c_3 was negatively shifted for about 0.2 eV (334.4 eV). The BE peak position shifting was generally due to the strong interactions between the prepared species (or due to the strong electronic effect) [17, 40], being an evidence of the chemical components variation in the final samples. Additionally, the BE peak area ratios of Pd^0 to that of Pd^{2+} for c_1 , c_2 and c_3 were roughly estimated to be 4.7, 5.5 and 0.7, respectively, further indicating that more amount of metallic Pd were formed in c_2 , being favorable to the electrocatalytic activity improvement of a Pd-based catalyst towards EOR [41].

3.2 SEM and TEM characterization

Photos for the starting material of NAA and all calcined products are presented in figure a of Fig.3. Apparently, the calcined products of NAA-300, NAA-500 and NAA-700, respectively, delivered a dark brown, a bright black and a dark gray color.



(c)

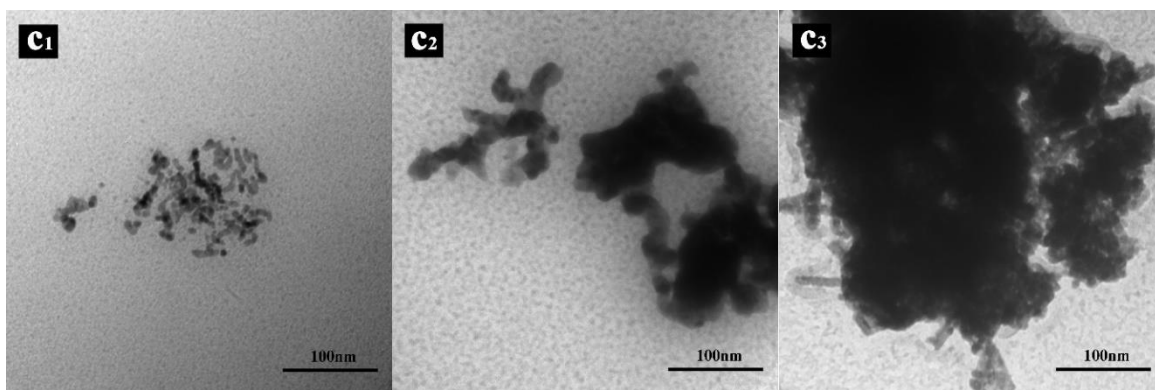


Figure 3. (a) Photos for the starting material of NAA as well as its calcination products. NAA-300, NAA-500 and NAA-700 represented the products calcined at 300 °C, 700 °C and 700 °C for 2 h in air atmosphere, respectively. (b) SEM images with scales of 1 μm and 100 nm for catalyst c_1 , c_2 and c_3 . Image c_1 , c_2 and c_3 corresponded to catalyst c_1 , c_2 and c_3 . (c) TEM images with a scale of 100 nm for all prepared catalysts. Image c_1 , c_2 and c_3 corresponded to catalyst c_1 , c_2 and c_3 .

The difference in the colors of the calcined products indirectly suggested that the chemical components of the calcined products were rather different from each other. SEM images with various scales for all prepared catalysts are shown in figure b of Fig.3. A huge particle with a rock-shaped surface was clearly displayed in c_1 which, as revealed by image c_1 with a scale of 100 nm, was constructed by numerous aggregated small particles. While for c_2 (image c_2), a beehive-shaped huge particle was exhibited clearly. Apparently, except for numerous nanoparticles with a size less than 40 nm, a large number of cavities appeared in c_2 which was very conducive to the flowing of the electrolyte solution.

That is to say, the contacting area between the nanoparticle catalysts and the electrolyte solution could be remarkably enlarged when using catalyst c_2 , which, due to the greatly reduced overpotential, was beneficial to the electrocatalytic performance improvement of an electrocatalyst. For c_3 , a large particle with a scorched earth-shaped surface morphology was exactly presented. As revealed by image c_3 with a scale of 100 nm, besides several agglomerates, some petal-shaped particles appeared in c_3 indicating that c_3 was also constituted by a great deal of small particles. TEM images for all prepared catalysts are presented in figure c of Fig.3. For c_1 , many strip-shaped particles with a width of about 3.8 nm were displayed suggesting that the huge particles observed in the SEM images were piled up by numerous smaller strip-shaped nanoparticles. In the case of c_2 , some irregular aggregated particles were well displayed implying that the beehive-shaped huge particles appearing in c_2 were also accumulated by nanoparticles. For c_3 , several large agglomerates were exhibited distinctly which substantially indicated that the severe aggregation of nanoparticles occurred in forming c_3 . Apparently, in above cases, no well-defined regular particles were presented in the TEM images, which was different from the previously reported TEM images of the Pd-based catalysts [25].

3.3. Electrocatalytic performance towards EOR

The cyclic voltammetry (CV) curves of various catalysts coated GC electrodes, which were measured in 1M KOH +1M ethanol at the scan rate of 50 mVs^{-1} , are collected in Fig.4a. Apparently, for each catalyst coated GC electrode, the CV curve was composed by a forward electrooxidation peak and a backward electrooxidation peak demonstrating that all newly prepared catalysts had an evident electrocatalytic activity towards EOR. In general, the forward electrooxidation peak (denoted as peak f) appearing in the positive potential scanning was attributed to the direct electrooxidation of ethanol molecules, and the backward electrooxidation peak (denoted as peak b) emerging in the negative potential scanning was mainly originated from the electro-oxidation of the intermediates that were produced during the direct electro-oxidation of ethanol molecules [42]. The peak current densities of peak f and peak b in the case of using c_1 , c_2 and c_3 were measured to be 6.3 and 5.2 mA cm^{-2} , 25.0 and 19.7 mA cm^{-2} , 1.1 and 1.1 mA cm^{-2} , respectively. Thus, the peak current density of peak f on c_2 was nearly, respectively, 4 and 22 time larger than that of peak f on c_1 and c_3 , implying that c_2 had a significant electrocatalytic activity towards EOR as compared to other two catalysts. In addition, the EOR peak current density ratios of peak f to peak b were, respectively, calculated to be about 1.21, 1.27 and 1.0 when using c_1 , c_2 and c_3 , which strongly suggested that c_2 had better anti poisoning capability (or better tolerance) and catalytic activity to the intermediate carbonaceous species as compared to other two catalysts [43].

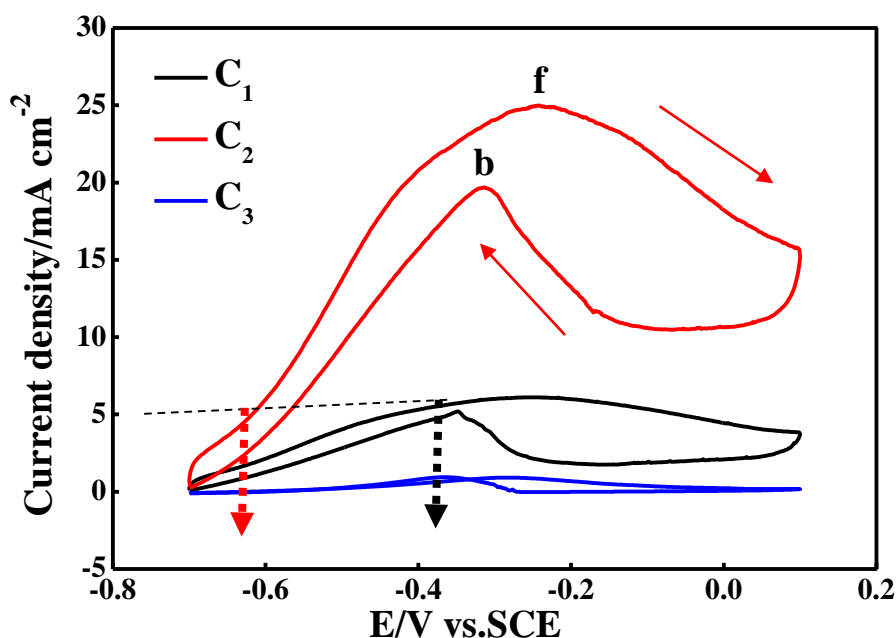
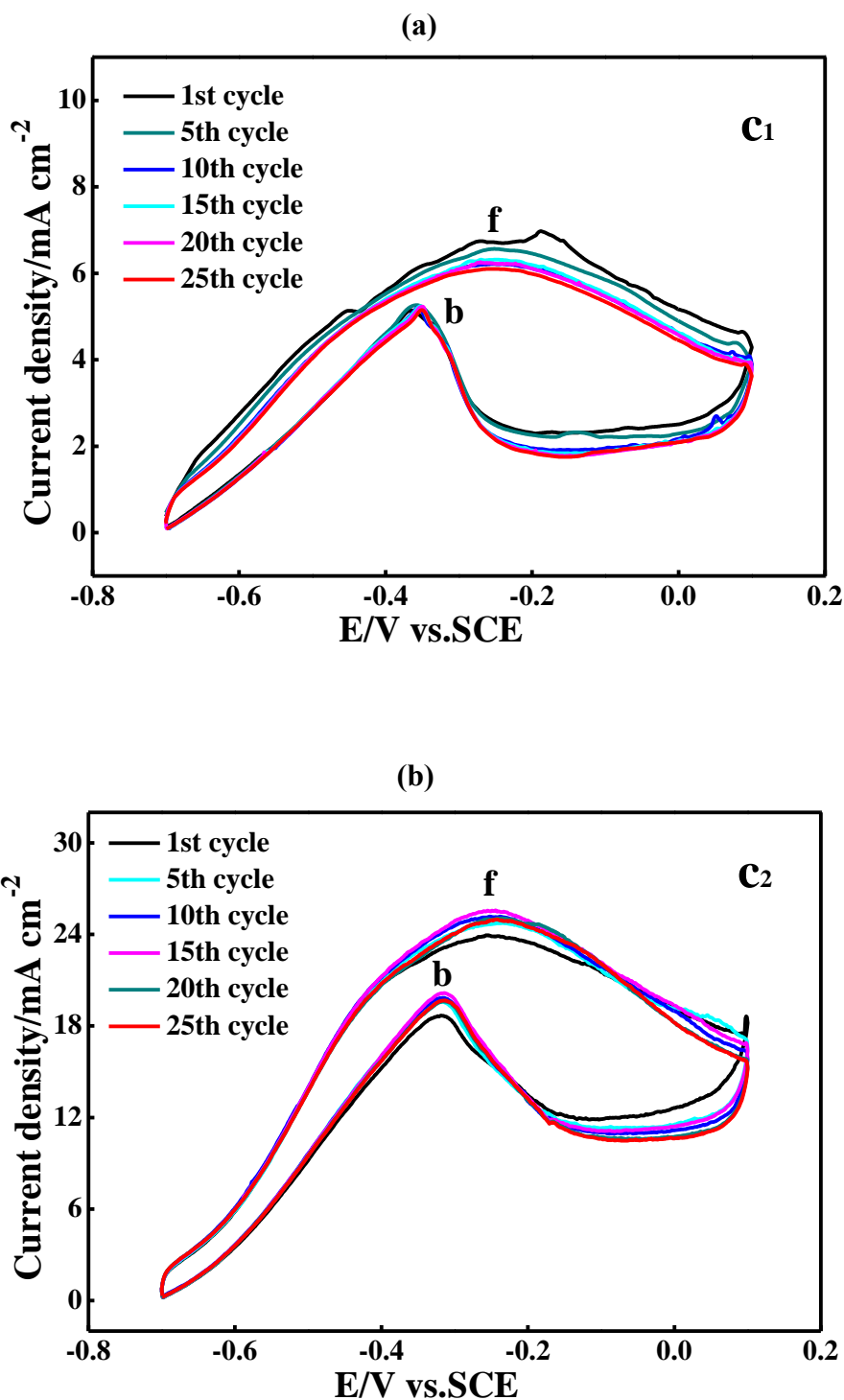


Figure 4a. CV curves measured on various catalysts coated GC electrode at the scan rate of 50 mV s^{-1} in which the electrolyte solution was 1M KOH+1M ethanol. Curve c_1 , c_2 and c_3 corresponded to the case of using catalyst c_1 , c_2 and c_3 .

Moreover, the over-potential of EOR was greatly reduced by using c_2 . For example, the electrode potentials corresponding to 5 mA cm^{-2} of peak f measured on c_2 and c_1 were -0.62 V and -0.38 V , respectively. That is, as compared to the case of using c_1 , the EOR over-potential was reduced for about 240 mV through using c_2 to achieve the current density of 5 mA cm^{-2} . Here, the electrocatalytic performance of c_3 towards EOR was not compared with that of c_1 and c_2 due to its much lower peak current density. Therefore, the largest peak current density as well as the lowest EOR over-potential was delivered by c_2 among all prepared catalysts.



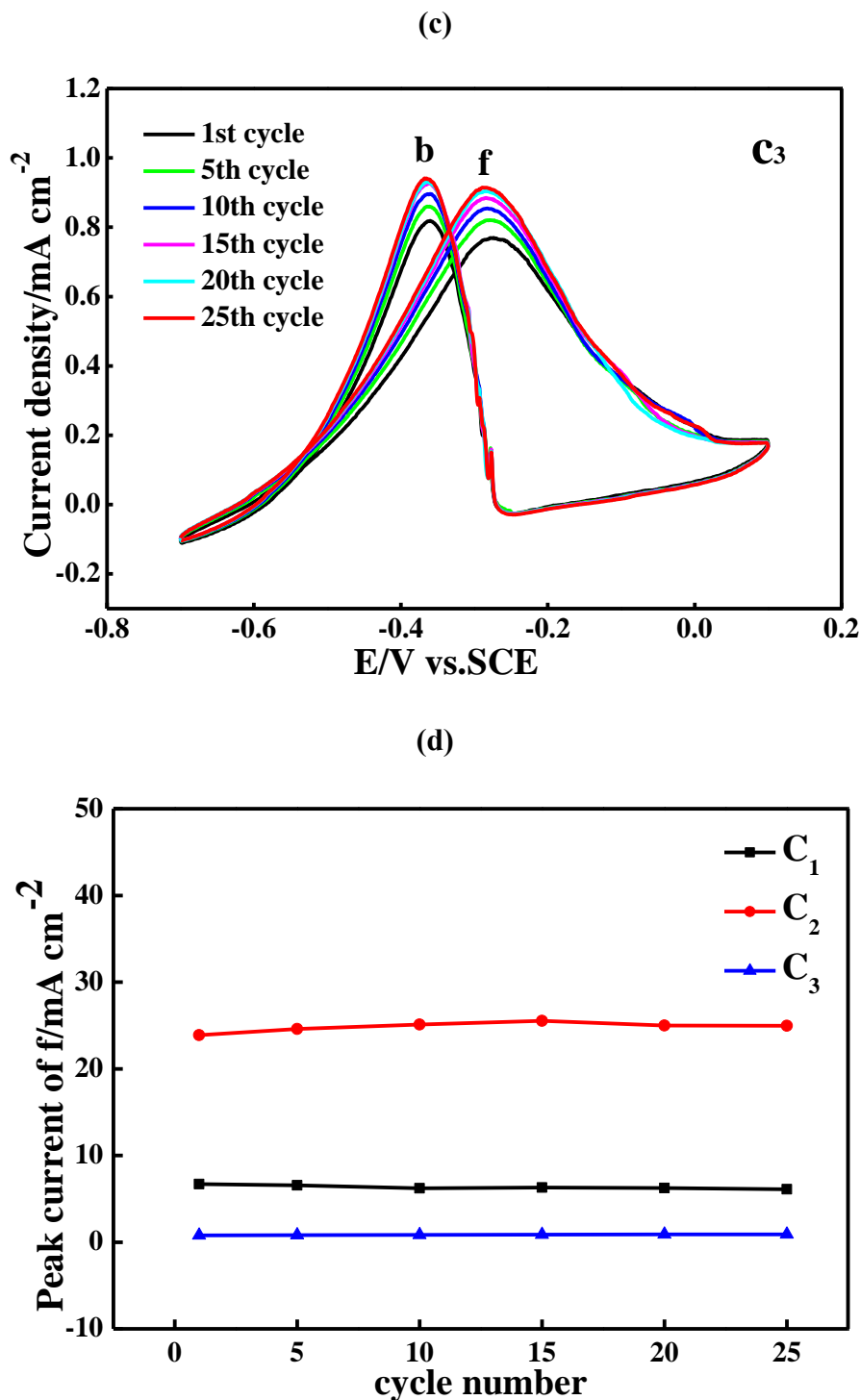


Figure 4b. CV curves recorded at the 1, 5, 10, 15, 20 and 25 cycles which were measured on various catalysts coated GC electrodes in the electrolyte solution of 1M KOH+1M ethanol at the scan rate of 50 mV s^{-1} . Figure a, b and c, respectively, corresponded to the case of using catalyst c_1 , c_2 and c_3 coated GC electrode. Figure d showed the curves describing the relationship between the peak current density of the peak f for EOR and the cycling number, and curve c_1 , c_2 and c_3 corresponded to the case of using catalyst c_1 , c_2 and c_3 coated GC electrode.

In the figures of Fig.4b, each catalyst coated GC electrode was cycled for consecutive 25 CV cycles in the solution of 1M KOH containing 1M ethanol at the scan rate of 50 mV s^{-1} . For c_1 (figure a

of Fig.4b), although no evident variation of the peak current density of peak b was found, the peak current density of peak f slightly decreased with increasing the cycling number. For instance, the EOR peak current density of peak f varied from 6.7 mA cm^{-2} at the first cycle to 6.1 mA cm^{-2} at the 25th cycle, showing no evident decay in the peak current density value. Interestingly, in the case of c_2 (figure b of Fig.4b), the peak current density of peak f firstly increased gradually with increasing the cycling number and then slightly declined with the cycling number, showing an first-up-and-then-down tendency, which was probably attributed to the special beehive-shaped surface morphology of c_2 . For c_3 (figure c of Fig.4b), the peak current density of peak f also gradually increased with increasing the cycle number, presenting a similar variation trend to that of c_2 , though the EOR peak current density value of c_3 was too lower relative to that of both c_1 and c_2 . The relationship between the peak current density of peak f and the cycling number was again plotted in figure d of Fig.4b from which the peak current density variation trend was exhibited clearly. In brief, no evident decay of the electrocatalytic activity of all prepared catalysts towards EOR was found in the cycling test, and amongst all as-synthesized catalysts, c_2 exhibited the best electrocatalytic activity towards EOR in terms of both cyclic stability and the peak current density.

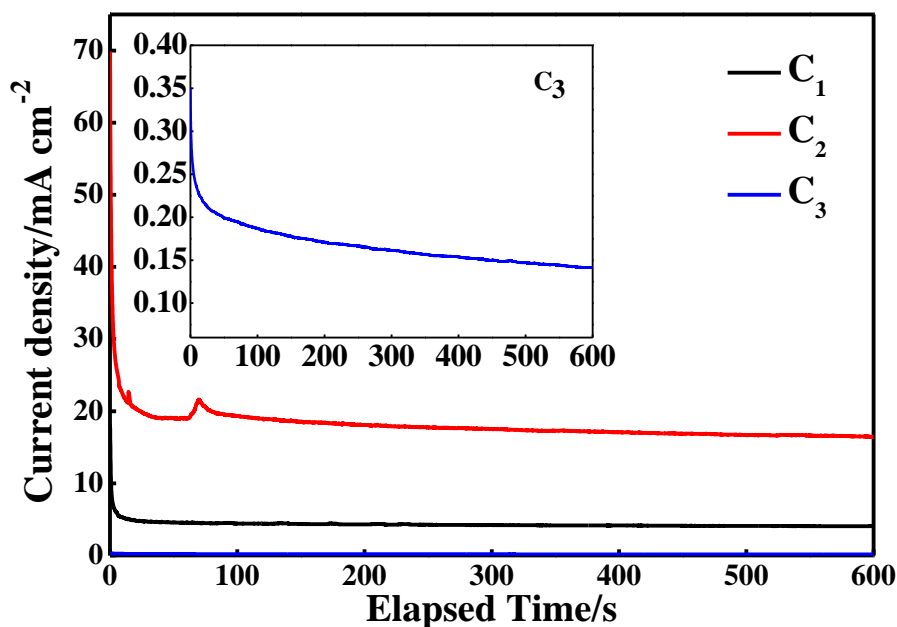


Figure 5. Chronoamperometry (CA) curves of EOR on various catalysts coated GC electrode which were measured at -0.25 V in the electrolyte solution of $1\text{M KOH}+1\text{M ethanol}$. Curve c_1 , c_2 and c_3 corresponded to the case of using catalyst c_1 , c_2 and c_3 coated GC electrode. The insert was the magnified CA curve of EOR when using c_3 coated GC electrode.

The electrocatalytic tolerance of an electrocatalyst is also an important factor which was directly relevant to the operating time of a catalyst in a practical fuel cell. The Chronoamperometry (CA) curves of EOR on all prepared catalysts were summarized in Fig.5 in which the electrode potential of each catalyst coated GC electrode was fixed to be -0.25V and the electrolyte solution was $1 \text{ M KOH} +1 \text{ M ethanol}$. For the i - t curves of both c_1 and c_2 , a rapid decline of the current density was

followed by a nearly straight current density platform. Generally, the sharp decline of the current density at the starting period of a CA test was resulted from the drastic capacitance current variation of the double-layer capacitance of an electrode [44]. And the straight current density platform, also called as polarized current or faradic current, was commonly attributable to the direct electrochemical oxidation of the ethanol molecules [45].

The inset of Fig.5 is the magnified CA curve of EOR on c_3 in which the current density was too small as compared to that of c_1 and c_2 , therefore, almost no polarized current density of EOR on c_3 was displayed in Fig.5. The polarized current densities of EOR on c_1 and c_2 at 600 s were, respectively, 4.1 and 16.5 mA cm^{-2} . It was worth emphasizing that the values of 4.1 and 16.5 mA cm^{-2} were all much higher than the previously reported data of 1.30 mA cm^{-2} [46]. That is to say, the electrocatalytic durability of c_2 and c_3 towards EOR was superior or comparable to that of the formerly reported EOR Pd-based catalyst.

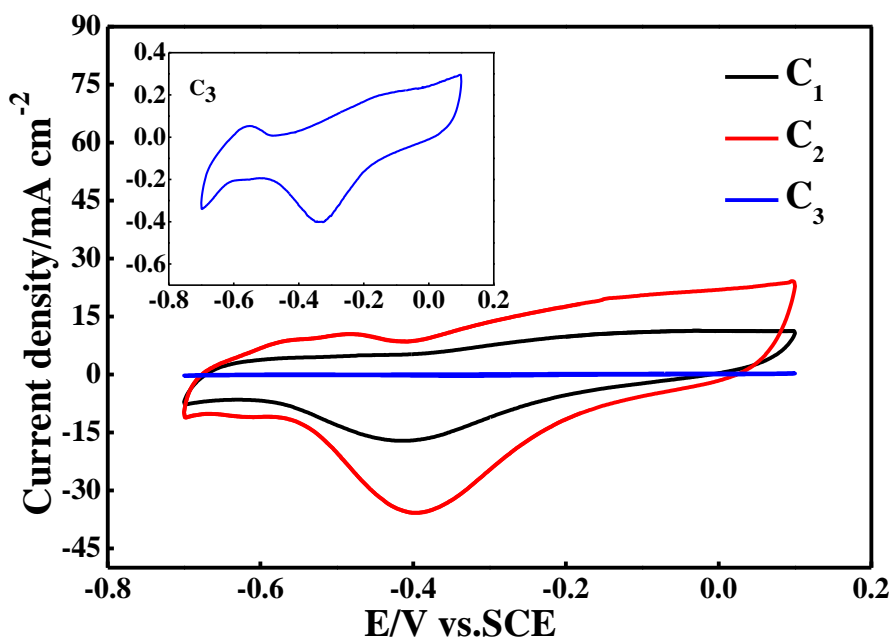


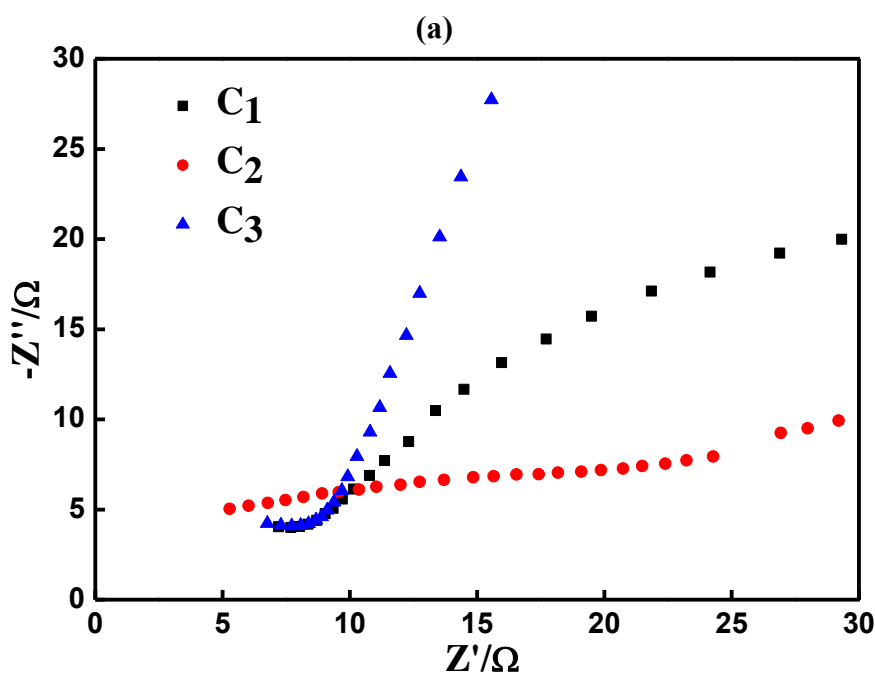
Figure 6. CV curves measured at the scan rate of 50 mV s^{-1} on various catalysts coated GC electrodes in 1 M KOH. Curve c_1 , c_2 and c_3 corresponded to the cases of using catalyst c_1 , c_2 and c_3 . The inner illustration at upper right corner is the magnified CV curve of using c_3 coated GC electrode.

To further discuss the electrocatalysis mechanism of all prepared catalysts towards EOR, the CV curves of all catalyst coated GC electrodes in 1 M KOH were recorded and the results are shown in Fig.6. For both c_1 and c_2 , an obvious electrochemical reduction peak was exhibited at -0.40 V , which, based on the previous work [47], should be stemmed from the electrochemical reduction of PdO, namely, $\text{PdO} + \text{H}_2\text{O} + 2\text{e}^- \leftrightarrow \text{Pd} + 2\text{OH}^-$. The inset of Fig.6 was the magnified CV curve of c_3 in which the electrochemical reduction peak assigned to the electrochemical reduction of PdO was also clearly displayed. However, the current density value measured on c_3 was too lower as compared to that measured on c_1 and c_2 , as a result, the CV curve recorded on c_3 as a straight line was exhibited in Fig.6.

Apparently, the largest CV peak area was delivered by c_2 among all as-synthesized prepared catalysts. That is, the largest amount of metallic Pd was electrochemically prepared on c_2 among all resultant catalysts since the CV peak area was generally proportional to the quantity of the electric charge consumed in an electrochemical reaction. Also, as shown by the figures of Fig.4b, the electrochemical oxidation of ethanol was usually started from -0.7V. In other words, prior to the EOR process, most PdO existing in the prepared catalysts have been electrochemically reduced to be metallic Pd. Thus, as compared to the case of using other catalysts, more amount of metallic Pd were formed on c_2 before the EOR process, consequently, c_2 delivered the best electrocatalytic activity towards EOR among all resultant catalysts. In addition, the electrochemical surface areas (ECSA) of all resultant catalysts were roughly calculated based on the CV curves shown in Fig.6 using the following equation [48],

$$\text{ECSA} = Q_{\text{PdO}} / (m \times C) \quad (1)$$

In above equation, Q_{PdO} was equal to the amount of electric charge that was used for the electrochemical reduction of monolayer PdO, and the value of Q_{PdO} was equal to the ratio value of the electrochemical reduction peak area to the potential scanning rate. And, m was the amount of the metallic Pd immobilized on the surface of the working electrode. C was a value of $424 \mu\text{C cm}^{-2}$. Evidently, c_2 , among all as-prepared catalysts, should deliver the largest value of ECSA due to its largest CV peak area when assuming other parameters in above equation for each catalyst were identical to each other. As a result, the ECSA for catalyst c_1 , c_2 and c_3 were approximately evaluated to be $79.2 \text{ m}^2 \text{ g}_{\text{Pd}}^{-1}$, $159.7 \text{ m}^2 \text{ g}_{\text{Pd}}^{-1}$ and $2.6 \text{ m}^2 \text{ g}_{\text{Pd}}^{-1}$, respectively. Notably, the ECSA values of both $79.2 \text{ m}^2 \text{ g}_{\text{Pd}}^{-1}$ and $159.7 \text{ m}^2 \text{ g}_{\text{Pd}}^{-1}$ were all greatly larger than that of the reported value of $16.02 \text{ m}^2 \text{ g}_{\text{Pd}}^{-1}$ [49], indicating that the electrocatalytic activities of c_1 and c_2 were superior to that of the formerly prepared EOR Pd-based catalyst.



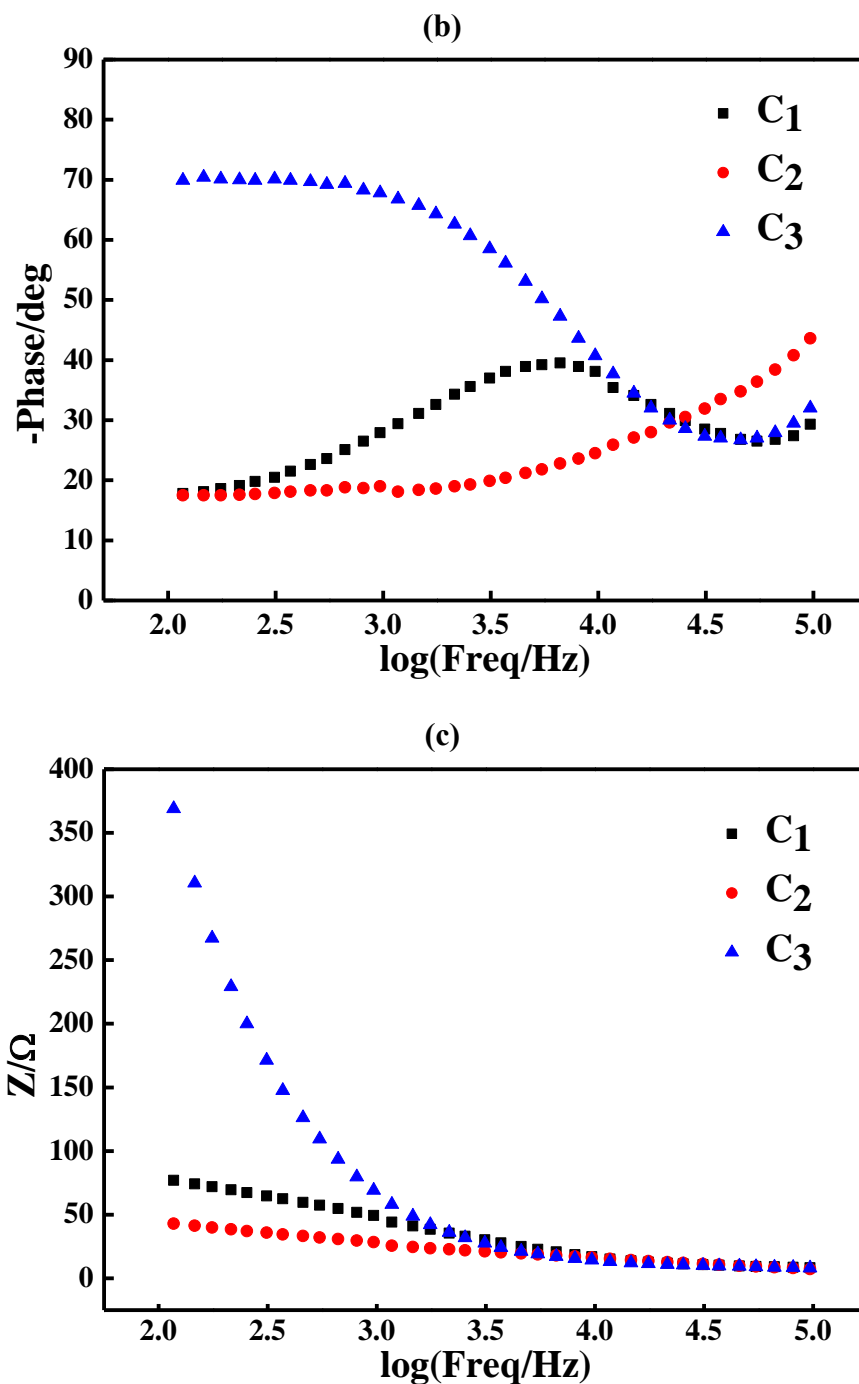


Figure 7. EIS results of all studied electrodes which were recorded in the electrolyte solution of 1 M KOH+1 M ethanol, in which curve c₁, c₂ and c₃ corresponded to the case of using c₁, c₂ and c₃ coated GC electrode. (a) Nyquist plots; (b) Bode plots; (c) Curves showing the relationship between the total impedance (Z) and frequency (f).

The Nyquist plots of all prepared catalysts are displayed in figure a of Fig.7. Generally, the Nyquist plot of an electrochemical reaction was constructed by a semicircle and a 45° line [50]. And approximately, the diameter value of the semicircle corresponded to the charge transfer resistance value (R_{ct}) [50]. To one's surprise, in this case, no conventional semicircles were found in the whole testing frequency region which was probably due to special morphologies of all prepared catalysts. For

the Nyquist plots of c_1 and c_3 , a nearly straight line was presented in the higher frequency region. And, a curve line and an oblique line were, respectively, observed in the lower frequency region of the Nyquist plots for c_1 and c_3 , showing rather different diffusion behavior. Interestingly, in the case of c_2 , only a sloped line with a lower gradient was displayed in the whole frequency region. Apparently, the rather different Nyquist plot shapes should be originated from both the various surface morphologies and the different body structures of all prepared catalysts.

The Bode curves for all resultant catalysts are given in figure b of Fig.7. Evidently, for c_1 , a symmetric peak centered at about $\log f=3.77$ was displayed clearly. And for c_3 , a plateau with a phase angle close to -70° was distinctly exhibited in the $\log(f/\text{Hz})$ region ranging from $\log(f/\text{Hz})=2$ to $\log(f/\text{Hz})=3$ suggesting that in the lower frequency range catalyst c_3 mainly acted as a capacitor[51]. To one's surprise, for c_2 , a slow rising line was exhibited in the whole frequency region. The rather different shapes in the Bode plots substantially demonstrated that the microstructures of all prepared catalysts were quite different from each other, which was well consistent with the results of SEM and TEM observation (Fig.3). The curves describing the total resistances and the frequency are collected in figure c of Fig.7. In this figure, the curve shape of c_1 was very similar to that of c_2 , i.e., almost a straight line was presented in the whole testing frequency region. While for c_3 , a rapid declined line appearing in the relatively lower frequency region was followed by a straight line appearing in the higher frequency region. Obviously, in the total testing frequency region, the total resistance of using c_2 was much lower than that of using other two catalysts. For instance, the total resistance values of c_1 , c_2 and c_3 at 100 Hz were 78, 42 and 371 Ω , respectively. Thus, c_2 delivered the smallest total resistance value among all prepared catalysts, which should be mainly originated from its particular beehive-shaped morphology.

Summarily, the special beehive-shaped morphology, the smallest particle size, the highest amount of metallic Pd, the largest ECSA and the lowest total resistance value were analyzed as the major reasons rendering c_2 the superior electrocatalytic activity towards EOR among all catalysts.

4. CONCLUSIONS

For the first time, palladium and nickel (Pd_xNi_y) composite catalysts with a beehive-shaped morphology were successfully prepared via a pyrolysis method employing the calcined product of NAA as the nickel-containing precursor. The final catalysts prepared with the precursors of NAA-300, NAA-500 and NAA-700 were, respectively, nominated as catalyst c_1 , c_2 and c_3 . As revealed by the SEM images, all prepared catalysts exhibited rather different morphologies, and particularly, a beehive-shaped morphology was delivered by c_2 . The presence of metallic Pd, metallic Ni, NiO and carbon materials in all prepared catalysts was effectively indicated by XRD and XPS measurements. Most important of all, as indicated by the CV and CA tests, all prepared catalysts had an evident electrocatalytic activity for EOR. And among all newly prepared catalysts, c_2 showed a significant electrocatalytic activity towards EOR. As demonstrated by the CA test, the Faraday current density of EOR on c_2 at 600 s was about around 16.5 mA cm^{-2} , greatly higher than that of EOR measured on c_1 (4.2 mA cm^{-2}) or on c_3 (0.15 mA cm^{-2}). The higher content of Pd, the special beehive-shaped

morphology, the rather lower total resistance value and the relatively larger ECSA value were regarded as the main reasons providing c_2 with an excellent electrocatalytic activity towards EOR. Preparing a novel nickel precursor and presenting a simple way to fabricate Pd_xNi_y nanoparticle electrocatalyst with beehive-shaped morphology as well as producing a high electrocatalytic performance EOR catalyst of c_2 were the main dedications of this preliminary work.

ACKNOWLEDGEMENTS

The work was supported by the Technical Innovation Advanced Research Foundation of Hebei Normal University (L2018K03).

References

1. L. Xiong, X. Zhang, L. Chen, Z. Deng, S. Han, Y. Chen, J. Zhong, H. Sun, Y. Lian, B. Yang, X. Yuan, H. Yu, Y. Liu, X. Yang, J. Guo, M. Rummeli, Y. Jiao and Y. Peng, *Adv. Mater.*, 33 (2021) 2101741.
2. N.-Y. Huang, H. He, S. Liu, H.-L. Zhu, Y.-J. Li, J. Xu, J.-R. Huang, X. Wang, P.-Q. Liao and X.-M. Chen, *J. Am. Chem. Soc.*, 143 (2021) 17424.
3. H. Wang, J. Chen, Y. Lin, X. Wang, J. Li, Y. Li, L. Gao, L. Zhang, D. Chao, X. Xiao and J.-M. Lee, *Adv. Mater.*, 33 (2021) 2008422.
4. L. Lin, H. Li, Y. Wang, H. Li, P. Wei, B. Nan, R. Si, G. Wang and X. Bao, *Angew. Chem. Int. Ed.*, 60 (2021) 26582.
5. S. Bai, Y. Xu, K. Cao and X. Huang, *Adv. Mater.*, 33 (2021) 2005767.
6. S. Luo, L. Zhang, Y. Liao, L. Li, Q. Yang, X. Wu, X. Wu, D. He, C. He, W. Chen, Q. Wu, M. Li, E. Hensen and Z. Quan, *Adv. Mater.*, 33 (2021) 2008508.
7. G. Liu, W. Zhou, Y. Ji, B. Chen, G. Fu, Q. Yun, S. Chen, Y. Lin, P.-F. Yin, X. Cui, J. Liu, F. Meng, Q. Zhang, L. Song, L. Gu and H. Zhang, *J. Am. Chem. Soc.*, 143 (2021) 11262.
8. Z. Liang, L. Song, S. Deng, Y. Zhu, E. Stavitski, R. Adzic, J. Chen and J. Wang, *J. Am. Chem. Soc.*, 141 (2019) 9629.
9. X. Lao, M. Yang, J. Chen, L. Zhang and P. Guo, *Electrochim. Acta*, 374 (2021) 137912.
10. Y. Qiu, J. Zhang, J. Jin, J. Sun, H. Tang, Q. Chen, Z. Zhang, W. Sun, G. Meng, Q. Xu, Y. Zhu, A. Han, L. Gu, D. Wang and Y. Li, *Nat. Commun.*, 12 (2021) 5273.
11. S. Zhang, K. Liu, Z. Liu, M. Liu, Z. Zhang, Z. Qiao, L. Ming and C. Gao, *Nano Lett.*, 21 (2021) 1074.
12. Y. Liang, T. Ma, Y. Xiong, L. Qiu, H. Yu and F. Liang, *Nanoscale*, 13 (2021) 9960.
13. D. Martín-Yerga, G. Henriksson and A. Cornell, *Int. J. Hydrogen Energy*, 46 (2021) 1615.
14. Q. Yi and Q. Chen, *Electrochim. Acta*, 182 (2015) 96.
15. M. Obradovic, Z. Stancic, U. Lacnjevac, V. Radmilovic, A. Gavrilovic-Wohlmuther, V. Radmilovic and S. Gojkovic, *Appl. Catal., B*, 189 (2016) 110.
16. P.-F. Yin, M. Zhou, J. Chen, C. Tan, G. Liu, Q. Ma, Q. Yun, X. Zhang, H. Cheng, Q. Lu, B. Chen, Y. Chen, Z. Zhang, J. Huang, D. Hu, J. Wang, Q. Liu, Z. Luo, Z. Liu, Y. Ge, X.-J. Wu, X.-W. Du and H. Zhang, *Adv. Mater.*, 32 (2020) 2000482.
17. H. Wang, S. Jiao, S. Liu, H. Zhang, Y. Xu, X. Li, Z. Wang and L. Wang, *Chem. Eur. J.*, 27 (2021) 1.
18. Y. Shen, S. Lu, W. Xu, A. Lv, Z. Wang, H. Wang, G. Liu and Y. Zhang, *Electrocatalysis*, 11 (2020) 522.
19. M. Nguyen, M.-K. Nguyen, P. Pham, H. Huynh, H. Pham, C. Vo and S. Nguyen, *J. Electroanal. Chem.*, 888 (2021) 115180.

20. S. Gomroki, Z. Yavari, A. Abbasian and M. Noroozifar, *Int. J. Appl. Ceram. Technol.*, 18 (2021) 2099.
21. M. Hasan, S. Newcomb, J. Rohan and K. Razeed, *J. Power Sources*, 218 (2012) 148.
22. S. Shen, T. Zhao, J. Xu and Y. Li, *J. Power Sources*, 195 (2010) 1001.
23. J. Yu, Y. Ni and M. Zhai, *J. Phys. Chem. Solids*, 112 (2018) 119.
24. F. Bouhjar, L. Derbali, B. Marí and B. Bessais, *Int. J. Hydrogen Energy*, 45 (2020) 11492.
25. T. Maiyalagan and K. Scott, *J. Power Sources*, 195 (2010) 5246.
26. S. Chowdhury, T. Maiyalagan, S. Bhattacharya and A. Gayen, *Electrochim. Acta*, 342 (2020) 136028.
27. S. Chowdhury, M. Banik, A. Mahajan and S. Bhattacharya, *ChemistrySelect*, 5 (2020) 9848.
28. Z. Cao, X. Liu, X. Meng, L. Cai, J. Chen and P. Guo, *Colloids Surf., A*, 621 (2021) 126577.
29. M. Lusi, H. Erikson, K. Tammeveski, A. Treshchalov, A. Kikas, H.-M. Piirsoo, V. Kisand, A. Tamm, J. Aruvali, J. Solla-Gullon and J. Feliu, *Electrochim. Acta*, 394 (2021) 139132.
30. Q. Wu, X. Yang, Q. Wan, R. Zhao, J. He and J. Zhu, *Compos. Sci. Technol.*, 198 (2020) 108296.
31. J. Fu, M. Zhang, L. Jin, L. Liu, N. Li, L. Shang, M. Li, L. Xiao and Y. Ao, *Appl. Surf. Sci.*, 470 (2019) 543.
32. J. Leger, S. Rousseau, C. Coutanceau, F. Hahn and C. Lamy, *Electrochim. Acta*, 50 (2005) 5118.
33. M. Jitianu, M. Balasoiu, R. Marchidan, M. Zaharescu, D. Crisan and M. Craiu, *Int. J. Inorg. Mater.*, 2 (2000) 287.
34. T. Ma, X. Zhao, Y. Cao, Y. Wu, Y. Zhou and H. Chen, *Dyes Pigm.*, 173 (2020) 107992.
35. J. Zhang, Z. Xie, W. Li, S. Dong and M. Qu, *Carbon*, 74 (2014) 153.
36. J. Li, D. Yan, S. Hou, T. Lu, Y. Yao, D. Chua and L. Pan, *Chem. Eng. J.*, 335 (2018) 579.
37. S. Javanmardi, Sh. Nasresfahani and M. Sheikhi, *Mater. Res. Bull.*, 118 (2019) 11049.
38. T. Almeida, Y. Yu, A. Andrade and H. Abruna, *Electrochim. Acta*, 295 (2019) 751.
39. M. Taheri, M. Ghiaci and A. Shchukarev, *Appl. Organomet. Chem.*, 32 (2018) 4338.
40. Y. Zhou, M. Niu, S. Zhu, Y. Liang, Z. Cui, X. Yang and A. Inoue, *Electrochim. Acta*, 296 (2019) 397.
41. K. Ding, Y. Wang, H. Yang, C. Zheng, Y. Cao, H. Wei, Y. Wang and Z. Guo, *Electrochim. Acta*, 100 (2013) 147.
42. K. Ding, C. Li, Y. Zhang, L. Wang, B. Wei, X. Shi and X. He, *Int. J. Hydrogen Energy*, 43 (2018) 1523.
43. Y. Shen, S. Lu, W. Xu, A. Lv, Z. Wang, H. Wang, G. Liu and Y. Zhang, *Electrocatalysis*, 11 (2020) 522.
44. K. Ding, C. Li, Y. Zhang, L. Wang, B. Wei, X. Shi and X. He, *Int. J. Hydrogen Energy*, 43 (2018) 1523.
45. K. Ding, H. Yang, Y. Cao, C. Zheng, S. Rapole and Z. Guo, *Mater. Chem. Phys.*, 142 (2013) 403.
46. J. Qu, Z. Yang, J. Wang, Z. Liu and C. Xu, *Electrochim. Acta*, 389 (2021) 138767.
47. Z. Liang, T. Zhao, J. Xu and L. Zhu, *Electrochim. Acta*, 54 (2009) 2203.
48. J. Feng, Q. Zhang, A. Wang, J. Wei, J. Chen and J. Feng, *Electrochim. Acta*, 142 (2014) 343.
49. V. Mozafari and J. Parsa, *Int. J. Hydrogen Energy*, 45 (2020) 28847.
50. K. Ding, Z. Jia, Q. Wang, X. He, N. Tian, R. Tong and X. Wang, *J. Electroanal. Chem.*, 513 (2001) 67.